Quantitative identification of moisture sources over the Tibetan Plateau and the relationship between thermal forcing and moisture transport

Chen Pan[1,2,3,4], Bin Zhu[1,2,3,4], Jinhui Gao[1,2,3,4], Hanqing Kang[1,2,3,4], Tong Zhu[5,6]

[1]Key Laboratory for Aerosol-Cloud-Precipitation of China Meteorological Administration, Nanjing University of Information Science & Technology, Nanjing, China

[2]Collaborative Innovation Center on Forecast and Evaluation of Meteorological Disasters, Nanjing University of Information Science & Technology, Nanjing, China

[3]Key Laboratory of Meteorological Disaster, Ministry of Education (KLME), Nanjing University of Information Science & Technology, Nanjing, China

[4]Joint International Research Laboratory of Climate and Environment Change (ILCEC), Nanjing University of Information Science & Technology, Nanjing, China

[5]CIRA, Colorado State University, Fort Collins, Colorado, USA

[6]NOAA/NESDIS/STAR/JCSDA, College Park, Maryland, USA

Correspondence to: Bin Zhu (E-mail: binzhu@nuist.edu.cn; Tel.: 86-25-58699785)

Abstract

Despite the importance of the Tibetan Plateau (TP) to the surrounding water cycle, the moisture sources of the TP remain uncertain. In this study, the moisture sources of the TP are quantitatively identified based on a 33-year simulation with a horizontal resolution of 1.9°×2.5° using the Community Atmosphere Model version 5.1 (CAM5.1), in which atmospheric water tracer technology is incorporated. Results demonstrate that the major moisture sources differ over the southern TP (STP) and northern TP (NTP). During the winter, Africa, the TP, and India are the dominant source regions, contributing nearly half of the water vapour over the STP. During the summer, the tropical Indian Ocean (TIO) supplies 28.5±3.6 % of the water vapour over the STP and becomes the dominant source region. The dominant moisture source regions of the water vapour over the NTP are Africa (19.0±2.8 %) during the winter and the TP (25.8±2.4 %) during the summer. The overall relative contribution of each source region to the precipitation is similar to the contribution to the water vapour over the TP. Like most models, CAM5.1 generally overestimates the precipitation over the TP, yielding uncertainty in the absolute contributions to the precipitation. Composite analyses exhibit significant variations in the TIO-supplied moisture transport and precipitation over the STP during the summer alongside anomalous TP heating. This relationship between moisture transport from the TIO and the TP heating primarily involves the dynamic change in the TIO-supplied moisture flux, which further controls the variation in the TIO-contributed precipitation over the STP.

Key words: Tibetan Plateau · Heat source · Moisture source apportionment · Moisture transport

1. Introduction

The Tibetan Plateau (TP), the highest plateau in the world, has important effects on its surrounding and global weather and climate systems (Flohn 1957; Yeh et al. 1957). The TP acts as a barrier that splits the subtropical westerlies into two branches during the winter (Bolin 1950; Manabe and Terpstra 1974). In addition, the TP regulates large-scale circulation by acting as an elevated heat source during the summer (Yanai et al. 1992; Wu and Zhang 1998).

Many studies have suggested that the Asian summer monsoon (ASM) rainfall is related to heating over the TP. This heating leads to an upper tropospheric divergent flow and a low-level convergent flow above the TP that brings precipitation to Asia (Li and Yanai 1996; Duan and Wu 2005; Duan et al. 2008; Wu et al. 2012). The precipitation can further intensify the upper-level thermal high pressure over the TP through the release of latent heat of condensation, eventually enhancing the thermal pumping effect of the TP (Yanai and Wu 2006). Hsu and Liu (2003) noted that heating over the TP during both spring and summer created wave-like circulation, such as Rossby waves, which further affected the summer rainfall in East Asia. Duan et al. (2011), Xu et al. (2013), and Wang et al. (2014) found that the pattern of summer precipitation in China was related to variation in spring thermal forcing over the TP. Wang et al. (2008) suggested that increases in the temperature over the TP may result in more summer frontal rainfall over East Asia. Recently, Boos and Kuang (2010) suggested that the TP thermal forcing has a negligible effect on the southwest summer monsoon. Nevertheless, Xu et al. (2014) noted that even if this viewpoint was true, the TP heat source still greatly affects the convective precipitation over the TP.

The identification of dominant moisture sources is a topic of research worldwide. Numerous source apportionment methods, such as analytical models, isotopes, numerical atmospheric water tracers, and model sensitivity experiments, have been developed and applied in this research area (Gimeno et al. 2012). Recently, many studies have focused on the identification of moisture sources of atmospheric water over the TP. Using observation data and model sensitivity experiments, Dong et al. (2016) established a new moisture transport pathway in which moisture is lifted by convection over central-eastern India and is transported to the south-western TP by mid-tropospheric circulation. This moisture contributes ~50 % of the summer precipitation over the south-western TP. Using the Lagrangian FLEXible PARTicle (FLEXPART) dispersion model (Stohl and James 2004), Chen et al. (2012) found that a narrow band area, including the Indian subcontinent, the Arabian Sea (AS), and the Indian Ocean in the Southern Hemisphere, is the dominant moisture source of the water vapour over the TP. Using the same model, Sun and Wang (2014) suggested that, throughout the year, most of the rainfall over the eastern TP originated from the Eurasian continent, even though the contribution from oceanic sources is notable. Zhang et al. (2017) suggested that Eurasian land evaporation supplies more than 69 % of the annual precipitation over the western-central TP, while greater than 21 % originates from the ocean. Curio et al. (2015) calculated the water vapour flux towards the TP and suggested that ~40 % of precipitation over the TP originates from external moisture sources, while the remaining ~60 % originates from local moisture recycling. Wang et al. (2017) suggested that the annual variation in the summer precipitation over the southern TP is determined by remote moisture transport. Meanwhile, local surface evaporation has a non-negligible effect on the summer precipitation. Yang et al. (2006) used the $\delta^{18}O$ data to determine that the summer precipitation over the central and northern areas of the TP is mainly provided by local evaporation. Based on isotope-incorporated atmospheric models, Yao et al. (2013) suggested that continental recycling is an important moisture source on the TP during both winter and summer and that the Indian Ocean is the dominant moisture source during the summer. Gimeno et al. (2012) summarized the main disadvantages of each method that limit diagnostic studies of moisture sources. For instance, analytical models need simplified assumptions, isotope data are influenced by signal sensitivity, Lagrangian methods allow limited consideration of cloud processes, and sensitivity experiments suffer from non-linarites. In contrast, the Eulerian atmospheric water tracer (AWT) approach lacks these weaknesses and is an efficient method to quantitatively identify the moisture source regions of precipitation or water vapour over a certain region based on the detailed physical parameterizations of global or regional models (Koster et al. 1986; Numaguti 1999; Bosilovich and Schubert 2002; Sodemann et al. 2009; Knoche and Kunstmann 2013; Singh et al.

2016; Pan et al. 2017). However, this tracer method has never been used to determine the dominant moisture sources in the TP region.

The TP is a key area that influences its own water resource allocation and that of its downstream regions (Barnett et al. 2005; Xu et al. 2008). The ASM delivers abundant moisture from the tropical oceans to the TP (Xu et al. 2014), while the mid-latitude westerlies also control moisture over the TP (Bothe et al. 2011;). Further investigation is required to understand the moisture sources and transport processes in the TP region (Yang et al. 2014). Supplementary Fig. S1 shows the distribution of the deuterium isotope ratio (δD) in each month for 2006–2009 based on hydrogen-deuterium-oxygen (HDO) and H_2O data from the Tropospheric Emission Spectrometer (TES) (Beer et al. 2001). The value of δD is notably greater from May to July than during other months over the TP and its surrounding areas. The increase in evapotranspiration over the TP and the transport of tropical moist air during the summer are two probable explanations for this phenomenon (Worden et al. 2007). However, natural moisture from around the world is difficult to quantify via measurements. Quantitative atmospheric water source apportionment may provide new insights into moisture transport over the TP. The moisture that originates from the TP and external regions is quantitatively identified in this study using the AWT method implemented in a global atmosphere model. We study the distributions of AWTs to further explore the relationship between the TP heat source and moisture transport during the summer.

In this study, descriptions of the model, data, and methods are provided in Sect. 2. Evaluations of the simulation results, moisture source apportionment on the TP, the relationship between the TP summer heat source and moisture transport from the tropical ocean, and uncertainties in the AWT method are presented in Sects. 3.1–3.4, respectively. Finally, a summary is provided in Sect. 4.

2. Data and methods

2.1 Model

The Community Atmosphere Model version 5.1 (CAM5.1) (Neale et al. 2012), in which the tagged AWT method has been implemented, is used in this study. In this study, the chemistry mechanism is taken from the Model for Ozone and Related chemical Tracers, version 4 (Emmons et al., 2010), in which water vapour is invariant. In CAM5.1, the physical processes involved in the temporal evolutions of atmospheric water substances (water vapour, cloud droplets, cloud ice, rain, and snow) including deep convection, shallow convection, cloud macrophysics, cloud microphysics, advection, and vertical diffusion are simply expressed as

$$\frac{\partial q_k}{\partial t} + \frac{1}{\rho}\nabla \cdot [\rho \mathbf{u} q_k] = \left(\frac{\partial q_k}{\partial t}\right)_{\mathrm{dp}} + \left(\frac{\partial q_k}{\partial t}\right)_{\mathrm{sh}} + \left(\frac{\partial q_k}{\partial t}\right)_{\mathrm{macro}} + \left(\frac{\partial q_k}{\partial t}\right)_{\mathrm{micro}} + D(q_k) \quad (1)$$

$$\frac{\partial q_p}{\partial t} = \left(\frac{\partial q_p}{\partial t}\right)_{\mathrm{dp}} + \left(\frac{\partial q_p}{\partial t}\right)_{\mathrm{sh}} + \frac{1}{\rho}\frac{\partial(V_{\mathrm{q}} \rho q_p)}{\partial z} + \left(\frac{\partial q_p}{\partial t}\right)_{\mathrm{micro}} \quad (2)$$

where t is the time, $\mathbf{u}$ is the three-dimensional wind vector, ρ is the air density, D is the turbulent diffusion operator, z is the height, and V_{q} is the mass-weighted terminal fall speeds. q_k is the mass mixing ratio (MMR), which is replaced by q_{v}, q_{l}, and q_{i} when calculating for water vapour, cloud droplets, and cloud ice, respectively. $\left(\frac{\partial q_k}{\partial t}\right)_{\mathrm{dp}}$, $\left(\frac{\partial q_k}{\partial t}\right)_{\mathrm{sh}}$, $\left(\frac{\partial q_k}{\partial t}\right)_{\mathrm{macro}}$, and $\left(\frac{\partial q_k}{\partial t}\right)_{\mathrm{micro}}$ are the tendencies in deep convection, shallow convection, cloud macrophysics, and cloud microphysical processes, respectively. q_p indicates the MMR of rain (q_{r}) or the MMR of snow (q_{s}). $\left(\frac{\partial q_p}{\partial t}\right)_{\mathrm{dp}}$ and $\left(\frac{\partial q_p}{\partial t}\right)_{\mathrm{sh}}$ are the net production of precipitation in deep convection and shallow convection, respectively. $\left(\frac{\partial q_p}{\partial t}\right)_{\mathrm{micro}}$ is the grid-mean source/sink term for q_p in the cloud microphysics of CAM5.1.

The deep convection scheme is taken from Zhang and McFarlane (1995) and follows modifications presented by Richter and Rasch (2008) and Raymond and Blyth (1986, 1992). The shallow convection scheme is taken from Park and Bretherton (2009). The cloud macrophysics parameterization in CAM5.1 is described in Park et al. (2014). The cloud microphysical scheme is taken from Morrison and Gettleman (2008) but with modifications following Gettleman et al.

(2010). The moist turbulence scheme from Bretherton and Park (2009) is used to calculate the vertical diffusion of heat, moisture, momentum, and tracers in CAM5.1. The finite volume dynamical core is used in this study because of its excellent performance for tracer transport (Rasch et al. 2006). CAM5.1's simulations can be driven by offline meteorological fields instead of online calculations; these simulations are called the specified dynamics simulations of CAM5.1 (Lamarque et al. 2012). A procedure that allows for more accurate comparisons between measurements of atmospheric composition and simulated results (Lamarque et al. 2012), first developed in the Model of Atmospheric Transport and Chemistry (Rasch et al., 1997), is applied to input offline meteorological fields into CAM5.1. This procedure requires horizontal wind fields, air temperature, surface pressure, surface temperature, surface geopotential, surface horizontal stress, and sensible and latent heat fluxes. In this study, the Modern Era Retrospective analysis for Research and Applications (MERRA) datasets (Rienecker et al. 2011) are used to drive the CAM5.1 model; the datasets were recommended by Lamarque et al. (2012) and have a time resolution of 6 h. All the input fields are linearly interpolated at time-steps between the reading times to avoid jumps and are then used to drive the CAM5.1's parameterizations to generate the necessary variables and calculate the sub-grid-scale transport and hydrological cycle (Lamarque et al. 2012). The sub-stepping procedure (Lauritzen et al. 2011) and the atmospheric mass fixer algorithm from Rotman et al. (2004) are applied to ensure consistencies between the input and model-calculated velocity and mass fields in CAM5.1 (Lamarque et al. 2012).

The tagged AWT method is described in Pan et al. (2017) and is similar to that in Numaguti (1999), Bosilovich and Schubert (2002), and Knoche and Kunstmann (2013). The atmospheric water substances are "tagged" at their geographical source region, and the formations of these substances start with evaporation at the surface (Knoche and Kunstmann 2013). Within the source region, the surface emission of tagged water vapour equals the surface evaporation of regular water vapour; outside the source region, the emission is zero. Then, these tagged atmospheric water substances undergo a series of atmospheric processes that regular water substances experience, but these substances have no feedback on the dynamical and thermal fields and are separate from regular water substances in CAM5.1. Accordingly, the time evolutions of the tagged atmospheric water substances are expressed as

$$\frac{\partial q_{k,\mathrm{tg}}}{\partial t} + \frac{1}{\rho}\boldsymbol{\nabla}\cdot\left[\rho\mathbf{u}q_{k,\mathrm{tg}}\right] = \left(\frac{\partial q_{k,\mathrm{tg}}}{\partial t}\right)_{\mathrm{dp}} + \left(\frac{\partial q_{k,\mathrm{tg}}}{\partial t}\right)_{\mathrm{sh}} + \left(\frac{\partial q_{k,\mathrm{tg}}}{\partial t}\right)_{\mathrm{macro}} + \left(\frac{\partial q_{k,\mathrm{tg}}}{\partial t}\right)_{\mathrm{micro}} + D\left(q_{k,\mathrm{tg}}\right) \tag{3}$$

$$\frac{\partial q_{p,\mathrm{tg}}}{\partial t} = \left(\frac{\partial q_{p,\mathrm{tg}}}{\partial t}\right)_{\mathrm{dp}} + \left(\frac{\partial q_{p,\mathrm{tg}}}{\partial t}\right)_{\mathrm{sh}} + \frac{1}{\rho}\frac{\partial\left(V_{\mathrm{q}}\rho q_{p,\mathrm{tg}}\right)}{\partial z} + \left(\frac{\partial q_{p,\mathrm{tg}}}{\partial t}\right)_{\mathrm{micro}} \tag{4}$$

where $q_{k,\mathrm{tg}}$ indicates various MMRs of tagged water vapour, tagged cloud droplets, and tagged cloud ice; that is, $q_{\mathrm{v,tg}}$, $q_{\mathrm{l,tg}}$, and $q_{\mathrm{i,tg}}$. $q_{p,\mathrm{tg}}$ represents the MMR of tagged rain ($q_{\mathrm{r,tg}}$) or the MMR of tagged snow ($q_{\mathrm{s,tg}}$). The terms on the right-hand sides of Eqs. (3) and (4) are generalized for conciseness, and detailed equations and treatments for various tagged atmospheric water tracers are presented in Pan et al. (2017). In this study, the globe is divided into 25 tagged source regions, as shown in Fig. 1. Regions 1–11 are oceanic source areas, and regions 12–25 are terrestrial source areas. Similar to Knoche and Kunstmann (2013), precipitating tagged water does not remain "tagged" any longer as non-subsurface tagged water in our method. Tagged water is completely lost when it precipitates outside its source region; tagged precipitation returns as a newly tagged quantity to the model system when it precipitates inside its source region.

The simulation, with a latitudinal resolution of 1.9° and longitudinal resolution of 2.5°, begins on 01 January 1981, and the initial MMRs of the tagged substances are set to zero in this study. The resolution of the MERRA datasets that are used in this study are identical to those of CAM5.1, which are available on the Earth System Grid (https://www.earthsystemgrid.org/home.html) and are generated from the original resolution (1/2° × 2/3°) using a conservative re-gridding procedure used in MERRA and CAM (Lamarque et al. 2012). The simulation result for the first year is used for model spin up to attain stable initial concentrations of tagged water substances. We investigate the results from 1982 to 2014.

2.2 Water vapour data

The Atmospheric Infrared Sounder (AIRS) water vapour dataset (Tian et al. 2014) from 2003 to 2014, which has 1°×1° horizontal resolution, is used in this study to assess the water vapour results over the TP. Additionally, the third Tibetan Plateau Atmospheric Scientific Experiment (TIPEX III), which is supported by the China Meteorological Administration (CMA), conducted daily vertical measurements of wind, air temperature, and moisture over the TP and its surrounding areas from 21 June to 3 September 2014. Seventeen L-band rawinsonde and 5 Global Position System (GPS) pilot balloon observation stations were used, whose locations are marked in Fig. 2c and d. These data are applied to validate the vertical distribution of the simulated water vapour over the TP.

2.3 Precipitation data

Station-observed hourly precipitation over the TP for 1982–2013 is provided by the CMA. The number of stations was 57 in the 1980s and has increased to 156 at present. The locations of these stations are shown in Fig. 4c. In addition, the Global Precipitation Climatology Project (GPCP) version 2.2 combined precipitation dataset (Huffman and Bolvin 2011) for the period 1982–2014 and the Tropical Rainfall Measuring Mission (TRMM) 3A12 satellite rainfall dataset (Huffman et al. 2007) from 1998 to 2014 are applied to estimate the simulated precipitation in this study.

2.4 Atmospheric heat source

The apparent heat source (Q_1) and apparent moisture sink (Q_2), as defined in Yanai et al. (1973), are calculated to identify the variation in heating over the TP:

$$Q_1 = c_p \left(\frac{p}{p_0}\right)^{\kappa} \left(\frac{\partial \theta}{\partial t} + \vec{V} \cdot \nabla \theta + \omega \frac{\partial \theta}{\partial p}\right) \quad (5)$$

$$Q_2 = -L\left(\frac{\partial q_v}{\partial t} + \vec{V}\cdot\nabla q_v + \omega\frac{\partial q_v}{\partial p}\right) \tag{6}$$

where θ is the potential temperature; q_v is the specific humidity; $\vec{V}$ is the horizontal velocity; p is the pressure; $p_0 =$ 1000 hPa; ω is the vertical p velocity; $\kappa = R/c_p$, where R is the gas constant, and c_p is the specific heat at a constant pressure of dry air; and L is the latent heat of water vapourisation.

Accordingly, the integrated Q_1 and Q_2 from the tropopause pressure (p_{T}) to the surface pressure (p_{S}) are expressed as

$$\mathrm{V}Q_1 = \frac{1}{g}\int_{p_{\mathrm{T}}}^{p_{\mathrm{S}}} Q_1\, dp \tag{7.1}$$

$$\mathrm{V}Q_2 = \frac{1}{g}\int_{p_{\mathrm{T}}}^{p_{\mathrm{S}}} Q_2\, dp \tag{8.1}$$

where g is the gravitational acceleration. Equations (7.1) and (8.1) can also be expressed as follows:

$$\mathrm{V}Q_1 = LP + S + \frac{1}{g}\int_{p_{\mathrm{T}}}^{p_{\mathrm{S}}} Q_R\, dp \tag{7.2}$$

$$\mathrm{V}Q_2 = L(P - E) \tag{8.2}$$

where P, E, and S are the precipitation rate, evaporation rate, and sensible heat flux at the surface, respectively, and Q_R is the radiative heating rate. The CAM5.1-calculated $\mathrm{V}Q_1$ is compared to that from the National Centers for Environmental Prediction (NCEP) reanalysis data (Kalnay et al. 1996) in Supplementary Fig. S2.

The normalized $\mathrm{V}Q_1$ is used to identify the heating anomaly over the TP from 1982 to 2014:

$$\mathrm{I}Q_1 = \frac{\mathrm{V}Q_1 - \overline{\mathrm{V}Q}_1}{\sigma} \tag{9}$$

where $\overline{VQ}_1$ is the 33 year-averaged VQ_1, and σ is the standard deviation of VQ_1.

2.5 The false discovery rate method

The over-interpretation of multiple hypothesis tests is a common problem in atmospheric sciences, and controlling the false discovery rate (FDR) is a computationally straightforward method to prevent this problem (Wilks et al. 2016).

The FDR is the expected fraction of rejected local null hypotheses that are actually true (Benjamini and Hochberg 1995; Ventura et al. 2004; Wilks 2006, 2016). This approach first sorts the probabilities (denoted as p_i values, with $i = 1, 2, \ldots, N$.) from N local hypothesis tests in ascending order. These sorted probabilities are denoted using parenthetical subscripts, that is, $p_{(1)} \leq p_{(2)} \leq \cdots \leq p_{(N)}$. The local null hypotheses are rejected if the corresponding p_i values are no greater than a threshold level

$$p_{\mathrm{FDR}} = \max\left[p_{(i)}: p_{(i)} \leq \frac{i}{N}\alpha_{\mathrm{FDR}}\right], i = 1, 2, \ldots, N \tag{10}$$

where α_{FDR} is the chosen level for the FDR.

2.6 Moisture flux components

The moisture flux can be divided into a mean term and three anomalous terms (Wei et al. 2016):

$$qu = (\bar{q} + q')(\bar{u} + u') = \bar{q}\bar{u} + \bar{q}u' + \bar{u}q' + q'u' \tag{11}$$

$$qv = (\bar{q} + q')(\bar{v} + v') = \bar{q}\bar{v} + \bar{q}v' + \bar{v}q' + q'v' \tag{12}$$

where q is the water vapour content or the MMR of a water vapour tracer, u is the zonal wind speed, and v is the meridional wind speed. Here, the bars represent the 33-year mean, and the primes represent the deviation from the mean. The rightmost three terms in Eqs. (11) and (12) represent the respective effects on the moisture transport by dynamic processes ($\bar{q}u'$ and $\bar{q}v'$), thermodynamic processes ($\bar{u}q'$ and $\bar{v}q'$), and the covariation of humidity and wind ($q'u'$ and $q'v'$).

On a longer timescale, the hydrological balance in the atmosphere can be expressed as (Brubaker et al. 1993)

$$P - E = -\frac{1}{g}\nabla \cdot \int_{p_{\mathrm{T}}}^{p_s} q\,\vec{V} dp \tag{13}$$

The right-hand sides of Eqs. (11) and (12) are substituted into the right-hand side of Eq. (13) (Wang et al. 2017):

$$-\frac{1}{g}\nabla \cdot \int_{p_{\mathrm{T}}}^{p_s} q\,\vec{V} dp = -\frac{1}{g}\left[\nabla \cdot \int_{p_{\mathrm{T}}}^{p_s} \bar{q}\,\vec{V}_a dp + \nabla \cdot \int_{p_{\mathrm{T}}}^{p_s} \bar{q}\overrightarrow{V'}\,dp + \nabla \cdot \int_{p_{\mathrm{T}}}^{p_s} q'\,\vec{V}_a dp + \nabla \cdot \int_{p_{\mathrm{T}}}^{p_s} q'\,\overrightarrow{V'} dp\right] \tag{14}$$

where $\bar{q}$ and $\vec{V_a}$ are the 33-year-averaged water vapour (or water vapour tracer) amount and horizontal wind fields, respectively, and $\overrightarrow{V'}$ is the deviation from $\vec{V_a}$. The second and third terms on the right-hand side of Eq. (14) represent the convergence of moisture caused by dynamic and thermodynamic processes, respectively.

3. Results and discussion

3.1 Model assessments

A comparison between AIRS-measured and CAM5.1-simulated water vapour at 500 hPa is shown in Fig. 2. During the boreal winter (December, January, and February), the water vapour is no greater than 1 g kg^{-1} over the TP. During the summer (June, July, and August), a northward decreasing gradient in the water vapour at 500 hPa is present over the TP in both the AIRS measurements and CAM5.1 simulation. Overall, the pattern of the water vapour over the TP and its surrounding areas can be characterized by CAM5.1. The difference between the AIRS-measured and CAM5.1-simulated water vapour is generally within the standard deviation of the AIRS measurement over most of the TP, except that the simulated water vapour is overestimated over areas around (32.5° N, 95° E) during the summer.

Figure 3 shows a comparison between the station-observed and simulated specific humidity at altitudes from 2 to 16 km from July to August in 2014. The simulated specific humidity is sampled at the nearest grid-point around the corresponding station in CAM5.1. Although the simulated specific humidity is overestimated compared with the observations below 6 km for some areas of the southern TP, such as Nakqu, Lhasa, Shigatse, and Xichang, the vertical distribution of the water vapour over the TP is generally well characterized by CAM5.1 during the summer.

Figure 4a and b show a comparison between the GPCP and CAM5.1 precipitation during the winter. The winter precipitation is generally ~1 mm d^{-1} over the TP, and the centre of precipitation is located in the north-western TP region. Figure 4c–f show the distributions of the summer precipitation based on the CMA station observations, TRMM data, GPCP data, and CAM5.1 simulation results, respectively. CAM5.1 can adequately represent the spatial pattern of the summer precipitation but significantly overestimates the precipitation along the southern and south-eastern edges of the TP. In addition, a high precipitation centre over the north-western TP is observed in the TRMM data but does not occur in the GPCP data and CAM5.1 results. To assess the inter-annual variation in the simulated summer precipitation in the TP region, the GPCP data, TRMM data, and CAM5.1 results are interpolated onto the 156 CMA stations using the bilinear interpolation method, which are shown in Fig. 5a. The correlation between the CMA data and CAM5.1 results is 0.44 at a 95 % significance level, and the correlation between the GPCP data and CAM5.1 results is 0.79 at a 99 % significance level, suggesting that CAM5.1 can reasonably characterize the inter-annual variation in the summer precipitation over the TP.

In addition, wind fields and potential temperature derived from the NCEP data are used to assess the CAM5.1 results, as shown in Supplementary Fig. S3. Overall, the horizontal wind fields and potential temperature are adequately simulated by CAM5.1.

3.2 Sources of atmospheric moisture over the TP

Yao et al. (2013) reported that 35° N is the northern edge of the Indian summer monsoon. Moreover, Figs. 2 and 4 show that the water vapour and precipitation south of 35° N (southern TP, or STP) are generally greater than those north of 35° N (northern TP, or NTP) during summer, implying that the sources of atmospheric waters may differ for these two portions of the TP. The contributions of all the moisture sources to the water vapour and precipitation over the STP and NTP are quantified using the AWT method, as shown in Fig. 6.

3.2.1 Moisture source apportionment over the STP

Figure 6a and b show the 33-year-averaged monthly contribution and percentage contribution of each source region to the water vapour over the STP.

During the winter, the mean amount of water vapour is generally less than 3.5 kg m^{-2} over the STP. The dominant source regions are Africa, the TP, and India, and the absolute (percentage) contributions of these regions are 0.48±0.13 kg m^{-2} (15.1±3.5 %), 0.69±0.12 kg m^{-2} (22.0±4.1 %), and 0.32±0.12 kg m^{-2} (10.2±3.3 %), respectively. The most important oceanic source region is the northern Atlantic Ocean, which supplies 0.27±0.06 kg m^{-2} (8.7±1.7 %) of the water vapour. In addition, only ~30 % of the winter water vapour originates from the oceans, indicating that the winter water vapour over the STP is dominated by land-surface evaporation.

The moisture supplied from the tropical Indian Ocean (TIO), Bay of Bengal (BOB), and AS increases in May and considerably decreases after September. During the summer, the TIO becomes the most important source region of the water vapour over the STP, with an absolute (percentage) contribution of 4.64±0.94 kg m^{-2} (28.5±3.6 %). This is consistent with Chen et al. (2012), who found that the Indian Ocean in the southern tropics is a dominant moisture source of the water vapour over the TP. The absolute (percentage) contribution from the AS to the water vapour over the STP is 0.81±0.23 kg m^{-2} (5.1±1.6 %) and that from the BOB is 0.49±0.13 kg m^{-2} (3.0±0.8 %) during the summer. Chen et al. (2012) suggested that the AS is a dominant source region of the water vapour over the TP. The atmospheric water substances are “tagged” at their geographical source, but precipitating tagged water no longer remains “tagged” in the AWT method. A great loss of water vapour originating from the AS occurs en route (Sun and Wang 2014), likely explaining the difference between our results and those of Chen et al. (2012). The TP and India remain important source regions during the summer, with contributions of 2.93±0.48 kg m^{-2} (18.1±2.4 %) and 1.59±0.39 kg m^{-2} (9.7±1.6 %), respectively.

Figure 6e and f show the 33-year-averaged monthly contribution and percentage contribution of each source region to the precipitation over the STP. During winter, Africa, the TP, and India are the three most important source regions. Their absolute (percentage) contributions are 0.15±0.09 mm d^{-1} (16.7±5.8 %), 0.13±0.06 mm d^{-1} (16.5±6.1 %), and 0.14±0.09 mm d^{-1} (15.9±7.0 %), respectively. During the summer, the TIO is the most dominant source region, with a contribution of 2.69±0.68 mm d^{-1} (32.9±3.6 %). This result is consistent with that of Yao et al. (2013), who suggested that the Indian Ocean is the dominant moisture source when monsoons develop. The TP is an important source region, supplying 1.20±0.23 mm d^{-1} (14.9±2.0 %) of the precipitation. Similarly, Zhang et al. (2017) suggested that local surface evaporation supplies approximately 18 % of the summer precipitation over the western-central areas of the STP. Wang et al. (2017) also noted that local moisture is a substantial component of the summer precipitation over the STP. India is another important source region, contributing 0.97±0.31 mm d^{-1} (11.7±1.9 %) of the summer precipitation.

The overall relative contribution of each source region to the precipitation is similar to the contribution to the water vapour because the availability of water vapour is an important factor in forming and sustaining precipitation. Gimeno et al. (2012) noted that the global distribution of precipitation is similar to the distribution of the total column of water vapour.

3.2.2 Moisture source apportionment over the NTP

Figure 6c and d show the contribution and relative contribution of each source region to the water vapour over the NTP. Most of the water vapour over the NTP originates from evaporation from terrestrial source regions throughout the year. The mean percentage contribution from terrestrial source regions is less (59.3 %) during the winter and greater (80.9 %) during the summer, in contrast with the conditions over the STP because the NTP is influenced by westerlies, and the STP is affected by the ASM during the summer (Yao et al. 2013).

During the winter, Africa is the dominant source region, supplying 0.52±0.12 kg m^{-2} (19.0±2.8 %) of the water vapour. In addition, the TP and Europe are two important terrestrial source regions of the winter water vapour, with absolute (percentage) contributions of 0.39±0.08 kg m^{-2} (14.7±3.5 %) and 0.24±0.07 kg m^{-2} (8.7±1.9 %), respectively. Approximately 0.45±0.09 kg m^{-2} (16.5±3.2 %) of the winter water vapour over the NTP originates from the northern Atlantic Ocean, an important oceanic source region. The AS supplies 0.14±0.07 kg m^{-2} (4.8±1.9 %) of the water vapour over the NTP.

During the summer, the TP is the most important source region, supplying 2.81±4.7 kg m^{-2} (25.8±2.4 %) of the water vapour over the NTP. Evaporation from Europe and northern Asia contributes 18.6±4.1 % and 20.6±3.7 % of the water vapour, respectively. From June to September, the contribution of water vapour from the TIO is evidently greater than that in other months; correspondingly, its absolute (percentage) contribution is 0.66±0.29 kg m^{-2} (5.9±2.1 %). Additionally, the northern Atlantic Ocean supplies 0.57±0.08 kg m^{-2} (5.3±1.1 %) of the summer water vapour over the NTP.

As shown in Fig. 6g and h, the overall relative contribution of each source region to the precipitation is also similar to the contribution to the water vapour over the NTP. During the winter, Africa, the northern Atlantic Ocean, Europe, and the TP are the four major moisture source regions of the precipitation over the NTP, with contributions of 0.24±0.09 mm d^{-1} (25.2±3.7 %), 0.12±0.05 mm d^{-1} (13.7±3.7 %), 0.13±0.06 mm d^{-1} (12.9±3.0 %), and 0.08±0.03 mm d^{-1} (8.8±3.5 %), respectively. During the summer, the TP is the most dominant source region of the precipitation over the NTP, with an absolute (percentage) contribution of 0.67±0.15 mm d^{-1} (31.5±3.5 %). Based on isotope data, Yang et al. (2006) also suggested that the TP surface evaporation is important to the summer precipitation over the NTP, with a local recycling ratio of at least 46.9 %. In addition, Europe and northern Asia are other two important sources of the summer precipitation, with contributions of 0.27±0.11 mm d^{-1} (12.8±4.3 %) and 0.33±0.13 mm d^{-1} (15.3±4.1 %), respectively. Thomas et al. (2016) suggested that local and northwesterly air masses have been important moisture sources of the north-eastern TP over the past 30,000 years.

3.3 Relationship between the TP heating and moisture transport from the tropical Indian Ocean

The vertical integrated apparent heat source (VQ_1, see Eq. (7.2)) consists of the latent heat of precipitation (LP), surface sensible heat (S), and vertical integrated atmospheric radiation heating (VQ_R). Figure 5b shows the inter-annual evolution of the summer mean of VQ_1, VQ_2 and their component terms over the TP. The value of LP approximates that of VQ_1, and a high correlation (the correlation coefficient $r = 0.97$) exists between them. This result is consistent with He et al. (1987), who suggested that the heating over the TP mainly originates from the release of latent heat of condensation. S is less than LP and exhibits an indistinctive inter-annual variation relative to LP. Radiation heating is negative, and its absolute value is comparable to the surface sensible heat during the summer. All these results imply that the variation in the TP summer heat source is primarily associated with the change in precipitation. The evolution of the normalized VQ_1 (see Eq. (9)) over the TP during the summer of 1982–2014 is shown in Fig. 5c. The TP heat source is anomalously strong in 1987, 1988, 1995, 1998, and 2000, whereas 1986, 1997, 2002, 2006, and 2009 are years with anomalously weak heating over the TP.

The dominant moisture source region that leads to precipitation over the STP during the summer is the TIO (Fig. 6). We further studied the composite anomalies of precipitation contributions from the TIO over Asia in anomalous TP heating years, as shown in Fig. 7a and b. The STP generally receives less TIO-contributed precipitation in weak heating years and more TIO-contributed precipitation in strong heating years. Evaporation and moisture transport are two factors that affect the precipitation at a seasonal scale (Eq. 13). Supplementary Fig. S4 generally shows no significant difference in evaporation over the TIO between weak and strong TP heating years, implying that the change in evaporation over the TIO barely influences the summer precipitation over the STP. Similarly, Wei et al. (2016) found that the variation in Northeast Pacific evaporation barely influences the precipitation in California despite being the dominant source region of

California's precipitation. Figure 7c and d show the composite anomalies of the advective tendency of the TIO-contributed water vapour during the summer in anomalous TP heating years. Similar to the anomalies in the TIO-contributed precipitation (Fig. 7a and b), the inflow of TIO-contributed water vapour is significantly weaker (stronger) over the STP in weak (strong) heating years. All these results indicate that the anomalies in the TP summer heat source are accompanied by evident changes in water vapour transport from the TIO to the STP. The variation in the water vapour transport from the TIO significantly changes the precipitation over the STP. The relationship between the TP heat source and moisture transport from the TIO has been explained in previous studies—Duan and Wu (2005) and Wu et al. (2007) suggested that the TP thermal forcing can cause the tropical moisture to converge towards and rise over the TP, resulting in abundant rainfall. The latent heat of rainfall can further intensify the TP heat source (Yanai and Wu 2006).

Wind field and water vapour amount are two variables that control moisture transport (see Eqs. (11) and (12)), both of which are associated with the dynamic and thermodynamic structures of the atmosphere, and their relative importance varies over different scales and regions (Li et al. 2013; Wang et al. 2017). The aforementioned results demonstrate that moisture transport (or precipitation) from the TIO has a strong connection to the TP summer heat source and suggest further study of the relative importance of dynamic and thermodynamic variations in moisture transport from the TIO to the TP when anomalous TP summer heating occurs. Figure 8 shows the composite vertical distributions of the TIO-supplied moisture flux components on the right-hand sides of Eqs. (11) and (12) during the summer in anomalous TP heating years. The dynamic component ($\bar{q}u'$) of the TIO-contributed zonal moisture flux below 400 hPa significantly decreases (increases) over the STP and areas to the east in response to a weak (strong) TP heat source (Fig. 8a and b). Figure 8e and f show that the thermodynamic component ($\bar{u}q'$) of the TIO-contributed zonal moisture flux below 400 hPa also significantly decreases (increases) over areas between 90° and 100° E in the STP in weak (strong) TP heating years. Similarly, Fig 8c and d show significant variation in the dynamic component ($\bar{q}v'$) of the TIO-contributed meridional moisture flux over the STP and areas farther south in anomalous TP heating years. The thermodynamic component ($\bar{v}q'$)

of the TIO-contributed meridional moisture flux is evidently lower over the STP in weak heating years (Fig. 8g) but becomes greater in strong heating years (Fig. 8h). The covariations of humidity and wind ($q'u'$ and $q'v'$) are negligible quantities compared with the dynamic and thermodynamic components. Additionally, the absolute value of the dynamic components ($\bar{q}u'$ and $\bar{q}v'$) are evidently greater than those of the thermodynamic components ($\bar{u}q'$ and $\bar{v}q'$) over the STP, indicating that the variation in the TP summer heat source is more related to the dynamic change in moisture transport from the tropical ocean.

Figure 5d shows the time series of summer averaged anomalies of the CMA station-observed precipitation and the convergence of the TIO-contributed moisture flux caused by dynamic ($-\frac{1}{g}\nabla \cdot \int_{p_{\mathrm{T}}}^{p_s}(\bar{q})_{\mathrm{TIO}}\overrightarrow{V'}dp$) and thermodynamic ($-\frac{1}{g}\nabla \cdot \int_{p_{\mathrm{T}}}^{p_s}(q')_{\mathrm{TIO}}\vec{V}_a dp$) processes over the STP for 1982–2013. The correlation between precipitation and the dynamic component is 0.58, which is statistically significant at a 99 % confidence level. The correlation between precipitation and the thermodynamic component is 0.31, which is statistically significant at a 90 % confidence level. A high correlation exists between the TP summer heat source and LP (Fig. 5b). Therefore, Fig. 5d indicates that the variation in the TP summer heat source is primarily related to the dynamic change in the TIO-supplied moisture transport. Duan and Wu (2005) and Wu et al. (2007) suggested that mutually reinforcing roles exist between the TP heat source and the tropical moisture transport during the summer. Wu et al. (2012) noted that the TP heat source can intensify the ASM circulation, which strengthens the inflow of water vapour and eventually increases precipitation over the TP. Thus, the variation in TP summer heating is primarily related to the dynamic component of the TIO-contributed moisture flux.

3.4 Uncertainties

The results of the AWT method depend on the performance of the model in reproducing the hydrological cycle (Numaguti 1999). The comparisons between the observed and CAM5.1-simulated water vapour demonstrate that CAM5.1

can generally represent the water vapour amount over the TP and its surrounding areas, except that the water vapour amount over some portions of the STP is overestimated. Therefore, biases may exist in the results of moisture source apportionment to water vapour over these areas. The precipitation over the TP, especially over the southern margin of the TP during the summer, is overestimated in CAM5.1 (Fig. 4). Therefore, uncertainty exists in the absolute contribution of each source region to the precipitation over the TP in this study. However, the results for the percentage contributions to precipitation are consistent with those of previous studies (Yang et al. 2006; Yao et al. 2013; Thomas et al. 2016; Wang et al. 2017; Zhang et al. 2017), facilitating meaningful studies of the quantitative moisture source apportionment to precipitation over the TP.

The coarse resolution of the model is a source of uncertainties and implies that the orographic barriers to moisture transport are not correctly represented. On the other hand, previous studies have suggested that global climate models, high-resolution regional climate models, and dynamical downscaling models overestimate the precipitation over the TP (Yu et al. 2010; Gao et al. 2012; Su et al. 2013), indicating that the models' parameterizations also bring uncertainties to the simulated results (Gao et al. 2012). Hence, simulations with higher resolution and further developments in models' parameterizations are still required to improve the performance when simulating moisture transport and precipitation, which should provide more accurate results from the AWT approach in the future.

Additionally, the surface evaporation flux from the MERRA dataset is used to drive CAM5.1 in this study, and thus the bias in the MERRA surface evaporation could have produced uncertainties in the results of the AWT method. Jiménez et al. (2011) suggested that the MERRA land evaporation is greater over southern and eastern Asia relative to other global estimates. Bosilovich et al. (2011) noted that, compared with other reanalysis datasets, the MERRA ocean evaporation is lower but much similar to observed data. Therefore, the bias in the MERRA surface evaporation may have produced the greater land contribution and lower oceanic contribution to atmospheric moisture over the TP in this study.

4. Conclusions

Although the TP is a key region that affects global water cycles, its moisture sources remain uncertain. We used the tagged AWT method implemented in CAM5.1 to quantitatively identify the moisture sources of water vapour and precipitation over the STP and NTP for 1982–2014. Africa, the TP, and India are the three dominant moisture sources of the winter water vapour over the STP, with absolute (percentage) contributions of 0.48±0.13 kg m^{-2} (15.1±3.5 %), 0.69±0.12 kg m^{-2} (22.0±4.1 %), and 0.32±0.12 kg m^{-2} (10.2±3.3 %), respectively. During the summer, the TIO becomes the dominant source region because of the development of the Asian summer monsoon, which supplies 4.64±0.94 kg m^{-2} (28.5±3.6 %) of the water vapour over the STP. During the winter, Africa is the dominant source region of the water vapour over the NTP, supplying 0.52±0.12 kg m^{-2} (19.0±2.8 %) of the water vapour. In addition, approximately 16.5±3.2 % of the winter water vapour originates from the northern Atlantic Ocean, which is an important oceanic source region. During the summer, the TP supplies 2.81±4.7 kg m^{-2} (25.8±2.4 %) of the water vapour over the NTP and becomes the most important source region. The overall relative contribution of each source region to the precipitation is similar to the contribution to the water vapour over the TP.

The TIO is the dominant moisture source of both the water vapour and precipitation over the STP in the summer. Meanwhile, the TP heat source is primarily associated with the release of latent heat of precipitation during the summer. Thus, we further investigated the relationship between the TP summer heating and the moisture transport from the TIO and found that water vapour transport from the TIO to the STP and the TIO-contributed precipitation over the STP significantly decrease (increase) in years with anomalously weak (strong) summer TP heating. However, the surface evaporation over the TIO generally exhibits no evident changes between strong and weak heating years. These results imply that anomalies in the TP summer heat source are related to changes in moisture transport from the TIO rather than to its surface evaporation. After dividing the TIO-supplied moisture transport flux into dynamic and thermodynamic components, we found that anomalies in the TP summer heating are primarily related to the dynamic component of moisture transport from the TIO. This dynamic component further controls the variation in the TIO-contributed precipitation over the STP.

Acknowledgements

This work was supported by the National Key Research and Development Program of China (2016YFA0602003), the National Natural Science Foundation of China (Grant No. 91544229), and the projects of China Special Fund for Meteorological Research in the Public Interest (GYHY201406001).

References

Barnett TP, Adam JC, Lettenmaier DP (2005) Potential impacts of a warming climate on water availability in snow-dominated regions. Nature 438: 303–309. doi:10.1038/nature04141

Beer R, Glavich TA, Rider DM (2001) Tropospheric emission spectrometer for the Earth Observing System's Aura satellite. Appl Opt 40: 2356–2367. doi:10.1364/AO.40.002356

Benjamini Y, Hochberg Y (1995) Controlling the false discovery rate: a practical and powerful approach to multiple testing. J Roy Stat Soc B 57: 289–300

Bolin B (1950) On the Influence of the Earth's Orography on the General Character of the Westerlies. Tellus 2: 184–195. doi:10.1111/j.2153-3490.1950.tb00330.x

Boos WR, Kuang Z (2010) Dominant control of the South Asian monsoon by orographic insulation versus plateau heating. Nature 463: 218

Bosilovich MG, Robertson FR, Chen J (2011) Global energy and water budgets in MERRA. J Climate 24: 5721–5739. doi:10.1175/2011JCLI4175.1

Bosilovich MG, Schubert SD (2002) Water vapor tracers as diagnostics of the regional hydrologic cycle. J Hydrometeorol 3: 149–165. doi:10.1175/1525-7541(2002)003<0149:WVTADO>2.0.CO;2

Bothe O, Fraedrich K, Zhu X (2011) Large-scale circulations and Tibetan Plateau summer drought and wetness in a high-resolution climate model. Int J Climatol 31: 832 846. doi:10.1002/joc.2124

Bretherton CS, Park S (2009) A new moist turbulence parameterization in the Community Atmosphere Model. J Climate 22: 3422–3448. doi:10.1175/2008JCLI2556.1

Brubaker KL, Entekhabi D, Eagleson PS (1993) Estimation of continental precipitation recycling. J Climate 6: 1077–1089. doi:10.1175/1520-0442(1993)006<1077:EOCPR>2.0.CO;2

Chen B, Xu XD, Yang S, Zhang W (2012) On the origin and destination of atmospheric moisture and air mass over the Tibetan Plateau. Theor Appl Climatol 110: 423–435. doi:10.1007/s00704-012-0641-y

Curio J, Maussion F, Scherer D (2015) A 12-year high-resolution climatology of atmospheric water transport over the Tibetan Plateau. Earth Syst Dynam 6: 109–124. doi:10.5194/esd-6-109-2015

Dong W, Lin Y, Wright JS, Ming Y, Xie Y, Wang B, Luo Y, Huang W, Huang J, Wang L, Tian L, Peng Y, Xu F (2016) Summer rainfall over the southwestern Tibetan Plateau controlled by deep convection over the Indian subcontinent. Nat Commun 7: 10925. doi:10.1038/ncomms10925

Duan A, Li F, Wang M, Wu G (2011) Persistent weakening trend in the spring sensible heat source over the Tibetan Plateau and its impact on the Asian summer monsoon. J Climate 24: 5671–5682. doi:10.1175/JCLI-D-11-00052.1

Duan AM, Wu GX (2005) Role of the Tibetan Plateau thermal forcing in the summer climate patterns over subtropical Asia. Clim Dynam 24: 793–807. doi:10.1007/s00382-004-0488-8

Duan AM, Wu GX, Liang XY (2008) Influence of the Tibetan Plateau on the summer climate patterns over Asia in the IAP/LASG SAMIL model. Adv Atmos Sci 25: 518–528. doi:10.1007/s00376-008-0518-2

Emmons LK, Walters S, Hess PG, Lamarque J-F, Pfister GG, Fillmore D, Granier C, Guenther A, Kinnison D, Laepple T, Orlando J, Tie X, Tyndall G, Wiedinmyer C, Baughcum SL, Kloster S (2010) Description and evaluation of the Model for Ozone and Related chemical Tracers, version 4 (MOZART-4). Geosci Model Dev 3: 43–67. doi:10.5194/gmd-3-43-2010

Flohn H (1957) Large-scale aspects of the “summer monsoon” in South and East Asia. J Meteorol Soc Jpn 75: 180–186

Gao X, Shi Y, Zhang D, Wu J, Giorgi F, Ji Z, Wang Y (2012) Uncertainties in monsoon precipitation projections over China: results from two high-resolution RCM simulations. Clim Res 52: 213–226. doi:10.3354/cr01084

Gettelman A, Liu X, Ghan SJ, Morrison H, Park S, Conley AJ, Klein SA, Boyle J, Mitchell DL, Li J-LF (2010) Global simulations of ice nucleation and ice supersaturation with an improved cloud scheme in the Community Atmosphere Model. J Geophys Res 115: D18216. doi:10.1029/2009JD013797

Gimeno L, Stohl A, Trigo RM, Dominguez F, Yoshimura K, Yu L, Drumond A, Durán-Quesada AM, Nieto R (2012) Oceanic and terrestrial sources of continental precipitation. Rev Geophys 50: RG4003. doi:10.1029/2012RG000389

He H, McGinnis JW, Song Z, Yanai M (1987) Onset of the Asian Summer Monsoon in 1979 and the Effect of the Tibetan Plateau. Mon Weather Rev 15: 1966–1995. doi:10.1175/1520-0493(1987)115<1966:OOTASM>2.0.CO;2

Hsu HH, Liu X (2003) Relationship between the Tibetan Plateau heating and East Asian summer monsoon rainfall. Geophys Res Lett 30: 2066. doi:10.1029/2003GL017909

Huffman GJ, Bolvin DT (2011) GPCP version 2.2 combined precipitation data set documentation. NASA Goddard Space Flight Center, Mesoscale Atmospheric Processes Laboratory and Science Systems and Applications, Inc

Huffman GJ, Bolvin DT, Nelkin EJ, Wolff DB, Adler RF, Gu G, Hong Y, Bowman KP, Stocker EF (2007) The TRMM multisatellite precipitation analysis (TMPA): Quasi-global, multiyear, combined-sensor precipitation estimates at fine scales. J Hydrometeorol 8: 38–55. doi:10.1175/JHM560.1

Jiménez C, Prigent C, Mueller B, Seneviratne SI, McCabe MF, Wood EF, Rossow WB, Balsamo G, Betts AK, Dirmeyer PA, Fisher JB, Jung M, Kanamitsu M, Reichle RH, Reichstein M, Rodell M, Sheffield J, Tu K, Wang K (2011) Global intercomparison of 12 land surface heat flux estimates. J Geophys Res 116: D02102. doi:10.1029/2010JD014545

Kalnay E, Kanamitsu M, Kistler R, Collins W, Deaven D, Gandin L, Iredell M, Saha S, White G, Woollen J, Zhu Y, Leetmaa A, Reynolds R, Chelliah M, Ebisuzaki W, Higgins W, Janowiak J, Mo KC, Ropelewski C, Wang J, Jenne R, Joseph D (1996) The NCEP/NCAR 40-year reanalysis project. B Am Meteorol Soc 77: 437–471. doi:10.1175/1520-0477(1996)077<0437:TNYRP>2.0.CO;2

Knoche HR, Kunstmann H (2013) Tracking atmospheric water pathways by direct evaporation tagging: A case study for West Africa. J Geophys Res-Atmos 118: 12345–12358. doi:10.1002/2013JD019976

Koster R, Jouzel J, Suozzo R, Russell G, Broecker W, Rind D, Eagleson P (1986) Global sources of local precipitation as determined by the NASA/GISS GCM. Geophys Res Lett 13: 121–124. doi: 10.1029/GL013i002p00121

Lamarque J-F, Emmons LK, Hess PG, Kinnison DE, Tilmes S, Vitt F, Heald CL, Holland EA, Lauritzen PH, Neu J, Orlando JJ, Rasch PJ, Tyndall GK (2012) CAM-chem: description and evaluation of interactive atmospheric chemistry in the Community Earth System Model. Geosci Model Dev 5: 369–411. doi:10.5194/gmd-5-369-2012

Lauritzen PH, Ullrich P A, Nair RD (2011) Atmospheric transport schemes: desirable properties and a semi-Lagrangian view on finite-volume discretizations. Numerical Techniques for Global Atmospheric Models, Lecture Notes in Computational Science and Engineering 80: 185–250. doi:10.1007/978-3-642-11640-7_8

Li C, Yanai M (1996) The onset and interannual variability of the Asian summer monsoon in relation to land–sea thermal contrast. J Clim 9: 358–375. doi:10.1175/1520-0442(1996)009<0358:TOAIVO>2.0.CO;2

Li L, Li W, Barros AP (2013) Atmospheric moisture budget and its regulation of the summer precipitation variability over the southeastern United States. Clim Dyn 41: 613–631. doi:10.1007/s00382-013-1697-9

Manabe S, Terpstra TB (1974) The effects of mountains on the general circulation of the atmosphere as identified by

–

–

Morrison H, Gettelman A (2008) A new two-moment bulk stratiform cloud microphysics scheme in the Community Atmosphere Model, version 3 (CAM3). Part I: Description and numerical tests. J Climate 21: 3642–3659. doi:10.1175/2008JCLI2105.1

Neale RB, Chen C-C, Gettelman A, Lauritzen PH, Park S, Williamson DL, Conley AJ, Garcia R, Kinnison D, Lamarque J-F, Marsh D, Mills M, Smith AK, Tilmes S, Vitt F, Morrison H, Gameron-Smith P, Collins WD, Iacono MJ, Easter RC, Ghan SJ, Liu X, Rasch PJ, Taylor MA (2012) Description of the NCAR Community Atmosphere Model (CAM5). NCAR Technical Note NCAR/TN-486+STR, 275 pp

Numaguti A (1999) Origin and recycling processes of precipitating water over the Eurasian continent: Experiments using an atmospheric general circulation model. J Geophys Res 104: 1957–1972. doi:10.1029/1998JD200026

–

Park S, Bretherton CS (2009) The University of Washington shallow convection and moist turbulence schemes and their impact on climate simulations with the Community Atmosphere Model. J Climate 22: 3449–3469. doi:10.1175/2008JCLI2557.1

Park S, Bretherton CS, Rasch PJ (2014) Integrating cloud processes in the Community Atmosphere Model, version 5. J Climate 27: 6821–6856. doi:10.1175/JCLI-D-14-00087.1

Rasch PJ, Coleman DB, Mahowald N, Williamson DL (2006) Characteristics of Atmospheric Transport Using Three Numerical Formulations for Atmospheric Dynamics in a Single GCM Framework. J Climate 19: 2243–2266. doi:10.1175/JCLI3763.1

Rasch PJ, Mahowald NM, Eaton BE (1997) Representations of transport, convection, and the hydrologic cycle in chemical transport models: Implications for the modeling of short-lived and soluble species. J Geophys Res 102: 28127–28138. doi:10.1029/97JD02087

Raymond DJ, Blyth AM (1986) A stochastic mixing model for nonprecipitating cumulus clouds. J Atmos Sci 43: 2708–2718. doi:10.1175/1520-0469(1986)043<2708:ASMMFN>2.0.CO;2

Raymond DJ, Blyth AM (1992) Extension of the stochastic mixing model to cumulonimbus clouds. J Atmos Sci 49: 1968–1983. doi:10.1175/1520-0469(1992)049<1968:EOTSMM>2.0.CO;2

Richter JH, Rasch PJ (2008) Effects of convective momentum transport on the atmospheric circulation in the community atmosphere model, version 3. J Climate 21: 1487–1499. doi:10.1175/2007JCLI1789.1

Rienecker MM, Suarez MJ, Gelaro R, Todling R, Bacmeister J, Liu E, Bosilovich MG, Schubert SD, Takacs L, Kim G-K, Bloom S, Chen J, Collins D, Conaty A, da Silva A, Gu W, Joiner J, Koster RD, Lucchesi R, Molod A, Owens T, Pawson S, Pegion P, Redder CR, Reichle R, Robertson FR, Ruddick AG, Sienkiewicz M, Woollen J (2011) MERRA: NASA’s Modern-Era Retrospective analysis for Research and Applications. J Climate 24: 3624–3648. doi:10.1175/JCLI-D-11-00015.1

Rotman DA, Atherton CS, Bergmann DJ, Cameron-Smith PJ, Chuang CC, Connell PS, Connel PS, Dignon JE, Franz A, Grant KE, Kinnison DE, Molenkamp CR, Proctor DD, Tannahill JR (2004) IMPACT, the LLNL 3-D global atmospheric chemical transport model for the combined troposphere and stratosphere: Model description and analysis of ozone and other trace gases. J Geophys Res 109: D04303. doi:10.1029/2002JD003155

Singh HA, Bitz CM, Nusbaumer J, Noone DC (2016) A mathematical framework for analysis of water tracers: Part 1: Development of theory and application to the preindustrial mean state. J Adv Model Earth Syst 8: 991–1013. doi:10.1002/2016MS000649

Sodemann H, Wernli H, Schwierz C (2009) Sources of water vapour contributing to the Elbe flood in August 2002—A tagging study in a mesoscale model. QJR Meteorol Soc 135: 205–223. doi:10.1002/qj.374

Stohl A, James P (2004) A Lagrangian analysis of the atmospheric branch of the global water cycle. Part I: Method description, validation, and demonstration for the August 2002 flooding in central Europe. J Hydrometeorol 5: 656–678. doi:10.1175/1525-7541(2004)005<0656:ALAOTA>2.0.CO;2

Su F, Duan X, Chen D, Hao Z, Cuo L (2013) Evaluation of the global climate models in the CMIP5 over the Tibetan Plateau. J Climate 26: 3187–3208. doi:10.1175/JCLI-D-12-00321.1

Sun B, Wang H (2014) Moisture sources of semiarid grassland in China using the Lagrangian particle model FLEXPART. J Climate 27: 2457–2474. doi:10.1175/JCLI-D-13-00517.1

Thomas EK, Huang Y, Clemens SC, Colman SM, Morrill C, Wegener P, Zhao J (2016) Changes in dominant moisture sources and the consequences for hydroclimate on the northeastern Tibetan Plateau during the past 32 kyr. Quaternary Sci Rev 131: 157–167. doi:10.1016/j.quascirev.2015.11.003

Tian B, Manning E, Fetzer E, Olsen E, Olsen E, Wong S (2014) AIRS/AMSU/HSB Version 6 Level 3 Product User Guide. Tech. Rep., Jet Propulsion Laboratory, Pasadena. https://disc.sci.gsfc.nasa.gov/AIRS/documentation/v6_docs/v6releasedocs-1/V6_L3_User_Guide.pdf

Ventura V, Paciorek JI, Risbey JS (2004) Controlling the Proportion of Falsely Rejected Hypotheses when Conducting Multiple Tests with Climatological Data. J Climate 17: 4343–4356. doi: 10.1175/3199.1

Wang B, Bao Q, Hoskins B, Wu G, Liu Y (2008) Tibetan Plateau warming and precipitation changes in East Asia. Geophys Res Lett 35: L14702. doi:10.1029/2008GL034330

Wang Z, Duan A, Wu G (2014) Time-lagged impact of spring sensible heat over the Tibetan Plateau on the summer rainfall anomaly in East China: case studies using the WRF model. Clim Dyn 42: 2885–2898. doi:10.1007/s00382-013-1800-2

Wang Z, Duan A, Yang S, Ullah K (2017) Atmospheric moisture budget and its regulation on the variability of summer precipitation over the Tibetan Plateau. J Geophys Res-Atmos 122: 614–630. doi:10.1002/2016JD02551

Wei J, Jin Q, Yang Z-L, Dirmeyer PA (2016) Role of ocean evaporation in California droughts and floods. Geophys Res Lett 43: 6554–6562. doi:10.1002/2016GL069386

Wilks DS (2006) On “field significance” and the false discovery rate. J Appl Meteor Climatol 45: 1181–1189. doi:10.1175/JAM2404.1

Wilks DS (2016) “The Stippling Shows Statistically Significant Grid Points”: How Research Results are Routinely Overstated and Overinterpreted, and What to Do about It. B Am Meteorol Soc 97: 2263–2273. doi:10.1175/BAMS-D-15-00267.1

Worden J, Noone D, Bowman K, Beer R, Eldering A, Fisher B, Gunson M, Goldman A, Herman R, Kulawik SS, Lampel M, Osterman G, Rinsland C, Rodgers C, Sander S, Shephard M, Webster CR, Lampel M (2007) Importance of rain evaporation and continental convection in the tropical water cycle. Nature 445: 528–532. doi:10.1038/nature05508

Wu G, Liu Y, He B, Bao Q, Duan A, Jin FF (2012) Thermal controls on the Asian summer monsoon. Sci Rep 2: 404. doi:10.1038/srep00404

Wu G, Liu Y, Wang T, Wan R, Liu X, Li W, Wang Z, Zhang Q, Duan A, Liang X (2007) The influence of mechanical and thermal forcing by the Tibetan Plateau on Asian climate. J Hydrol 8: 770–789. doi:10.1175/JHM609.1

Wu G, Zhang Y (1998) Tibetan Plateau forcing and the timing of the monsoon onset over South Asia and the South China Sea. Mon Weather Rev 126: 913–927. doi:10.1175/1520-0493

Xu X, Lu C, Ding Y, Shi X, Guo Y, Zhu W (2013) What is the relationship between China summer precipitation and the change of apparent heat source over the Tibetan Plateau? Atmos Sci Let 14: 227–234. doi:10.1002/asl2.444

Xu X, Lu C, Shi X, Gao S (2008) World water tower: An atmospheric perspective. Geophys Res Lett 35: L20815. doi:10.1029/2008GL035867

Xu X, Zhao T, Lu C, Guo Y, Chen B, Liu R, Li Y, Shi X (2014) An important mechanism sustaining the atmospheric" water tower" over the Tibetan Plateau. Atmos Chem Phys 14: 11287–11295. doi:10.5194/acp-14-11287-2014

Yanai M, Esbensen S, Chu JH (1973) Determination of bulk properties of tropical cloud clusters from large-scale heat and moisture budgets. J Atmos Sci 30: 611–627. doi:10.1175/1520-0469(1973)030<0611:DOBPOT>2.0.CO;2

Yanai M, Wu GX (2006) Effects of the Tibetan Plateau. In: Wang B (ed) The Asian monsoon. Springer, Berlin/Heidelberg, pp 514–549

Yanai MH, Li C, Song Z (1992) Seasonal heating of the Tibetan Plateau and its effects on the evolution of the Asian summer monsoon. J Meteorol Soc Jpn 70: 319–351

Yang K, Wu H, Qin J, Lin C, Tang W, Chen Y (2014) Recent climate changes over the Tibetan Plateau and their impacts on energy and water cycle: A review. Global Planet Change 112: 79–91. doi:10.1016/j.gloplacha.2013.12.001

Yang M, Yao T, Wang H, Tian L, Gou X (2006) Estimating the criterion for determining water vapour sources of summer precipitation on the northern Tibetan Plateau. Hydrol Process 20: 505–513. doi:10.1002/hyp.5918

Yao T, Masson-Delmotte V, Gao J, Yu W, Yang X, Risi C, Sturm C, Werner M, Zhao H, He Y, Ren W, Tian L, Shi C, Hou S (2013) A review of climatic controls on $\delta^{18}O$ in precipitation over the Tibetan Plateau: Observations and simulations. Rev Geophys 51: 525–548. doi:10.1002/rog.20023

Yeh TC, Lo SW, Chu PC (1957) The wind structure and heat balance in the lower troposphere over Tibetan Plateau and its surrounding. Acta Meteor Sin 28: 108–121

Yu ET, Wang HJ, Sun JQ (2010) A quick report on a dynamical downscaling simulation over China using the nested model. Atmos Oceanic Sci Lett 3: 325–329. doi:10.1080/16742834.2010.11446886

Zhang C, Tang Q, Chen D (2017) Recent Changes in the Moisture Source of Precipitation over the Tibetan Plateau. J. Climate 30: 1807–1819. doi:10.1175/JCLI-D-15-0842.1

Zhang GJ, McFarlane NA (1995) Sensitivity of climate simulations to the parameterization of cumulus convection in the Canadian Climate Centre general circulation model. Atmos Ocean 33: 407–446. doi:10.1080/07055900.1995.9649539

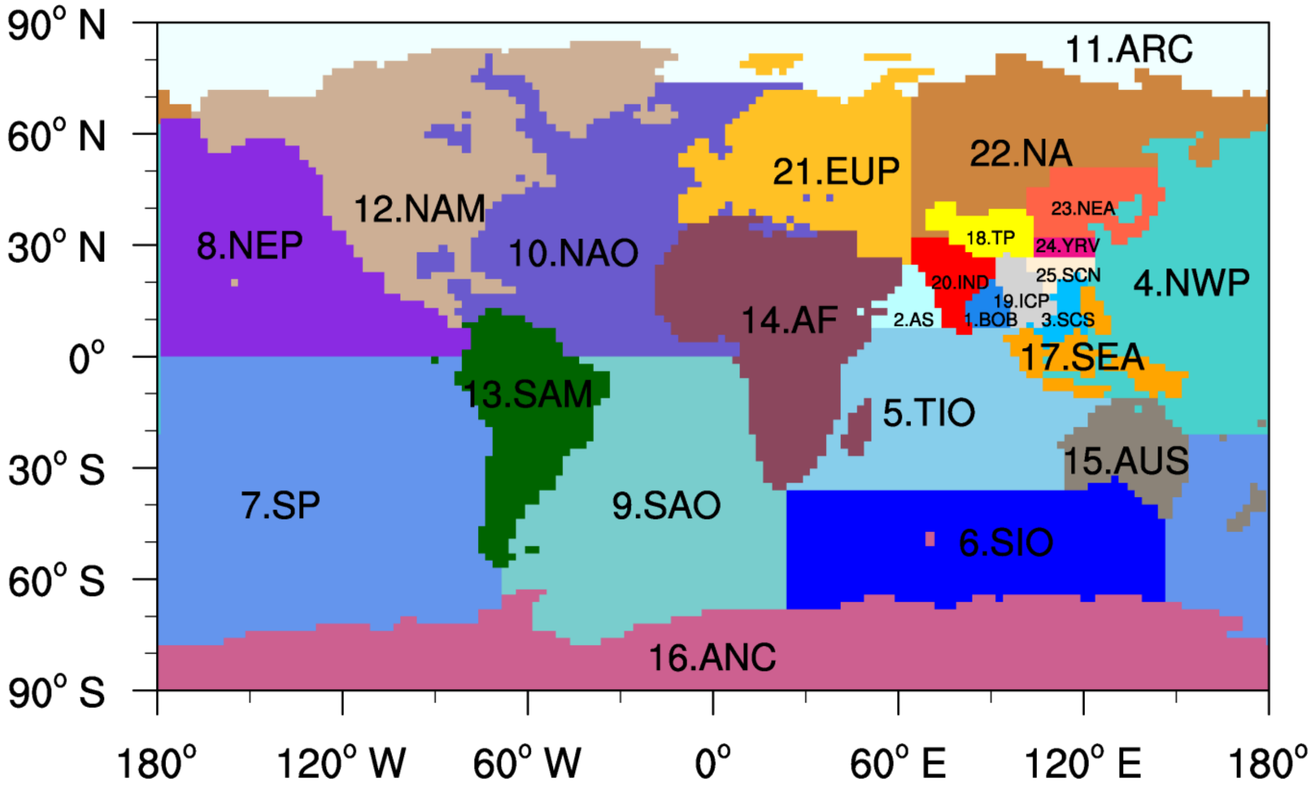

Fig. 1 Moisture source regions: (1) Bay of Bengal (BOB); (2) Arabian Sea (AS); (3) South China Sea (SCS); (4) Northwest Pacific (NWP); (5) tropical Indian Ocean (TIO); (6) southern Indian Ocean (SIO); (7) southern Pacific (SP); (8) Northeast Pacific (NEP); (9) southern Atlantic Ocean (SAO); (10) northern Atlantic Ocean (NAO); (11) Arctic Ocean (ARC); (12) North America (NAM); (13) South America (SAM); (14) Africa (AF); (15) Australia (AUS); (16) Antarctic (ANC); (17) Southeast Asia (SEA); (18) Tibetan Plateau (TP); (19) Indo-China Peninsula (ICP); (20) India (IND); (21) Europe (EUP); (22) North Asia (NA); (23) Northeast Asia (NEA); (24) Yangtze River valley (YRV); and (25) South China (SCN)

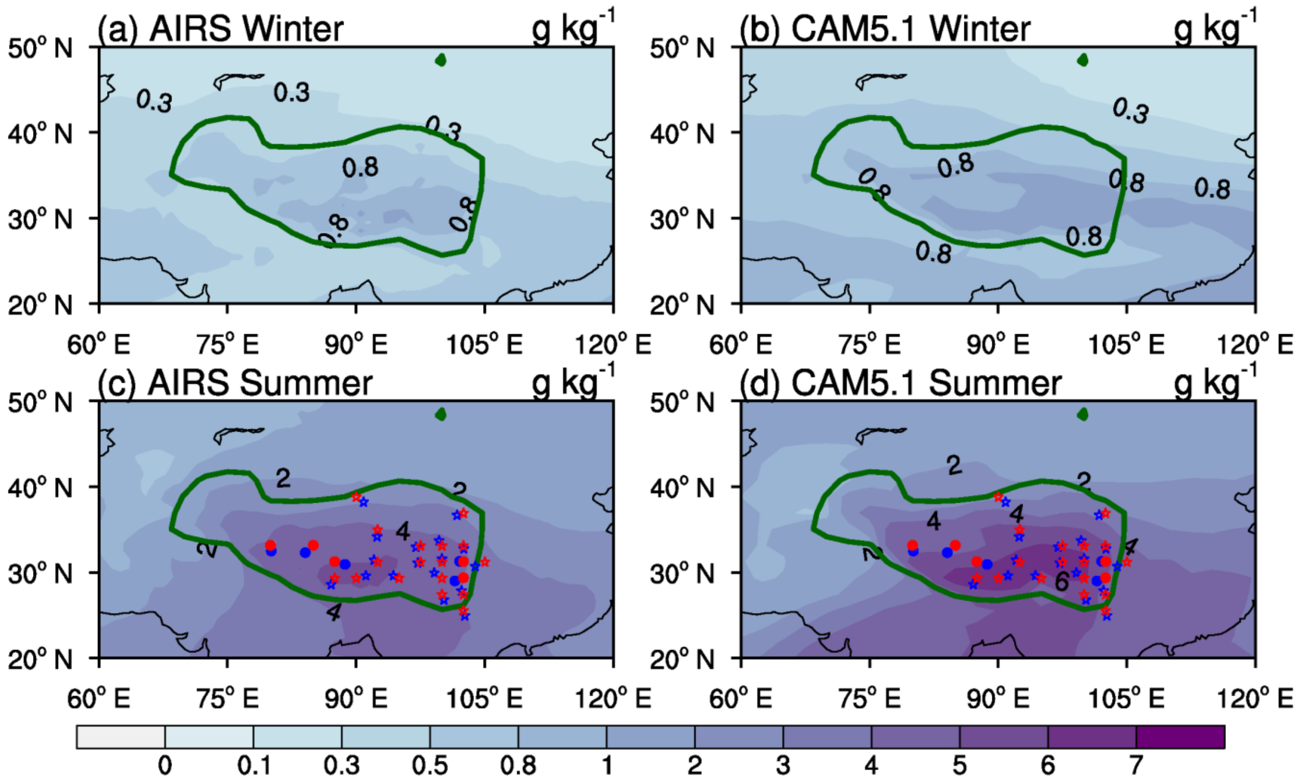

Fig. 2 Comparisons between the (a, c) AIRS-measured and (b, d) CAM5.1-modelled water vapour (units: g kg^{-1}) at 500 hPa during the winter and summer for 2003–2014. In Fig. 2c and d, the blue stars and circles represent the locations of 17 L-band rawinsonde and 5 Global Position System (GPS) pilot balloon observation stations, respectively. The red stars and circles represent the nearest grid-points around the corresponding stations in CAM5.1. The bold dark-green contours indicate an orographic height of 2000 m

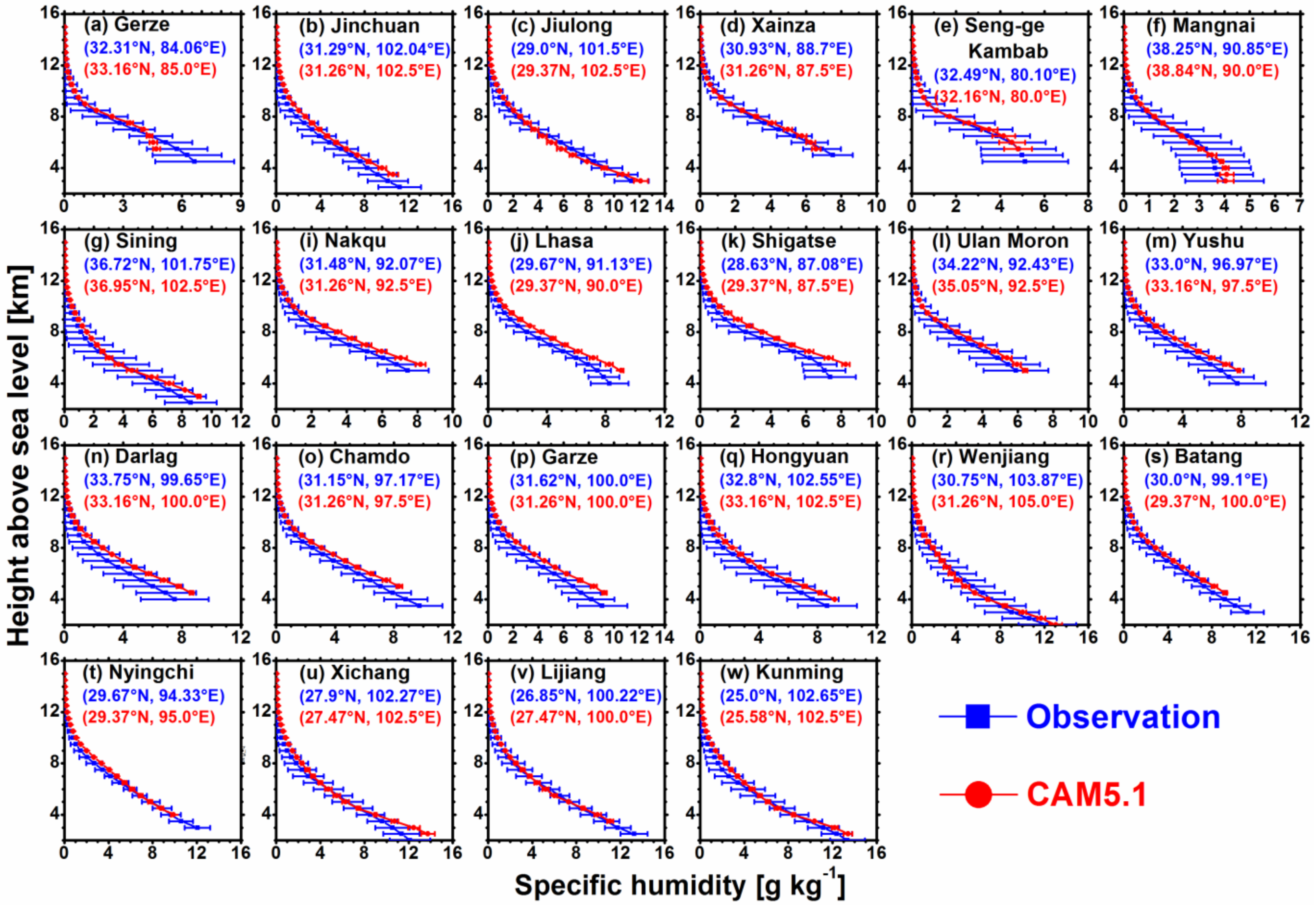

Fig. 3 Vertical profiles of the observed (22 stations) and simulated (CAM5.1) specific humidity (units: g kg^{-1}) during July and August of 2014. The blue diamonds and error bars represent the mean values and standard deviations of the observed specific humidity, respectively. Similarly, the red circles and error bars represent the mean values and standard deviations of the simulated specific humidity, respectively. The blue coordinates represent the locations of the observation stations, and the red coordinates denote the corresponding nearest grid points in CAM5.1. The locations of the 22 stations are shown in Fig. 2c and d

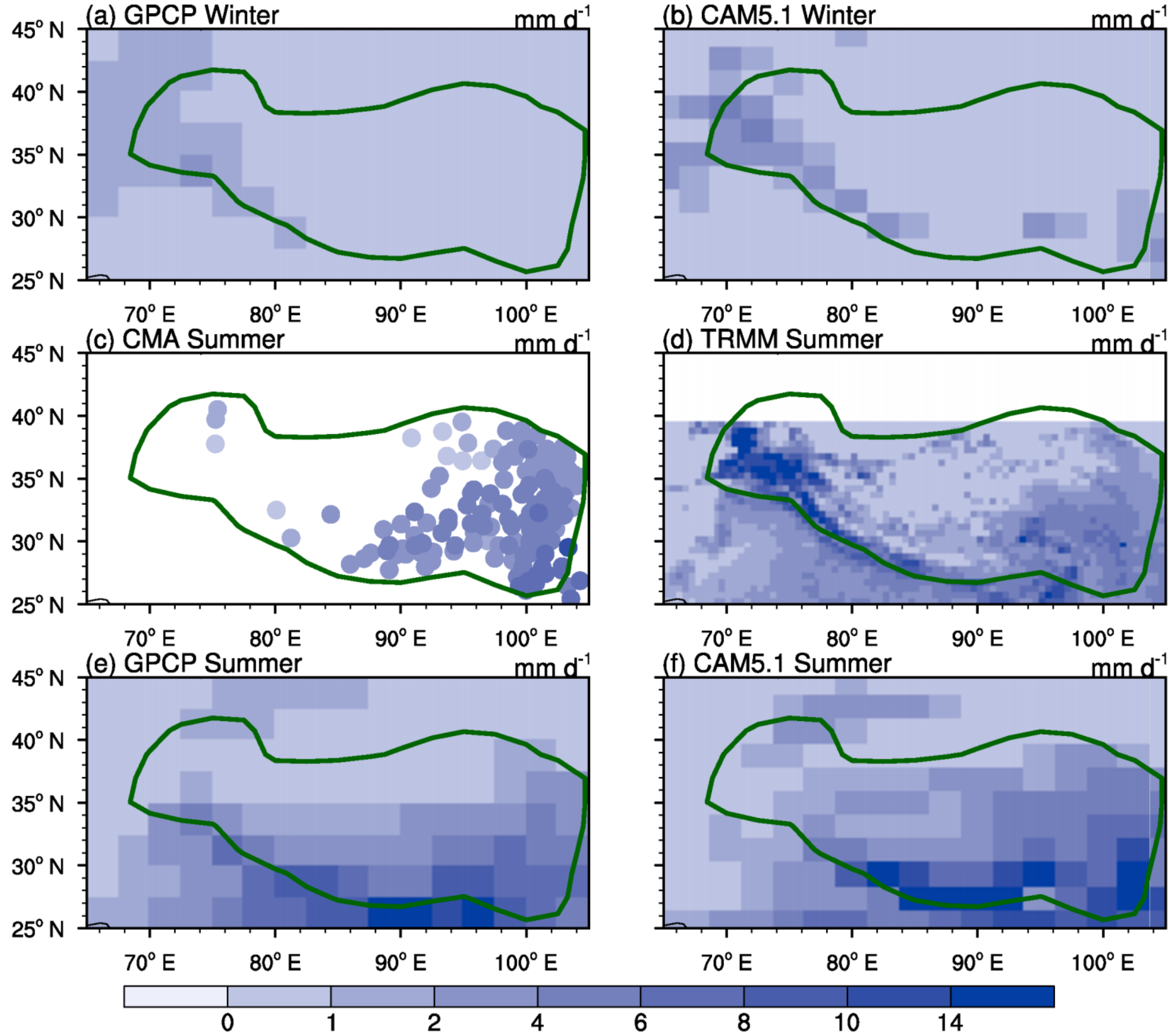

Fig. 4 Spatial distributions of the winter averaged precipitation (a) based on the GPCP data and (b) based on the CAM5.1 simulation from 1982 to 2014. Spatial distributions of the summer averaged precipitation (c) based on the CMA station observational data from 1982 to 2013, (d) based on the TRMM data from 1998 to 2014, (e) based on the GPCP data from 1982 to 2014, and (f) based on the CAM5.1 simulation from 1982 to 2014. All values are in units of mm d^{-1}. The dark-green contours indicate an orographic height of 2000 m

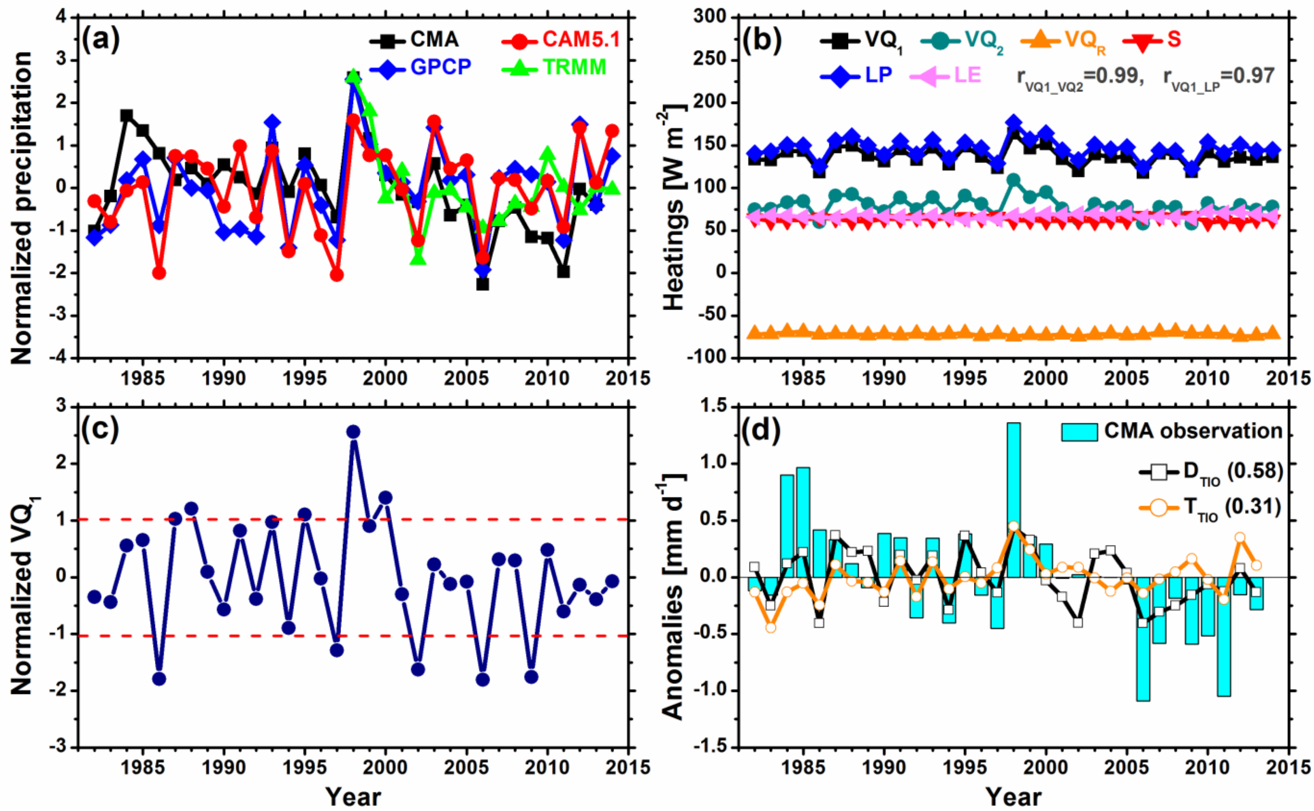

Fig. 5 (a) Time series of the normalized average summer precipitation of the CMA stations; the black, blue, green, and red curves represent the CMA station observations, GPCP, TRMM, and CAM5.1, respectively. (b) Time series of the vertically integrated apparent heat source (VQ_1, black), vertically integrated apparent moisture sink (VQ_2, dark-green), vertically integrated radiative heating (VQ_R, orange), surface sensible heat (S, red), latent heat of precipitation (LP, blue), and latent heat of evaporation (LE, pink) during the summer over the TP for 1982–2014, all with units of W m^{-2}. The correlation coefficient is $\mathrm{r}_{VQ_1\_VQ_2} = 0.99$ between VQ_1 and VQ_2, and the correlation coefficient is $\mathrm{r}_{VQ_1\_LP} = 0.97$ between VQ_1 and LP. (c) Time series of the normalized VQ_1 during the summer over the TP, which is derived from the CAM5.1 simulation between 1982 and 2014. (d) Time series of the averaged summer anomalies of the CMA observed precipitation and the convergence of the TIO-contributed moisture flux caused by dynamic (D_TIO) and thermodynamic (T_TIO) processes over the STP for the period of 1982–2013, all with units of mm d^{-1}. The values in brackets are correlation coefficients between the observed precipitation and corresponding variables

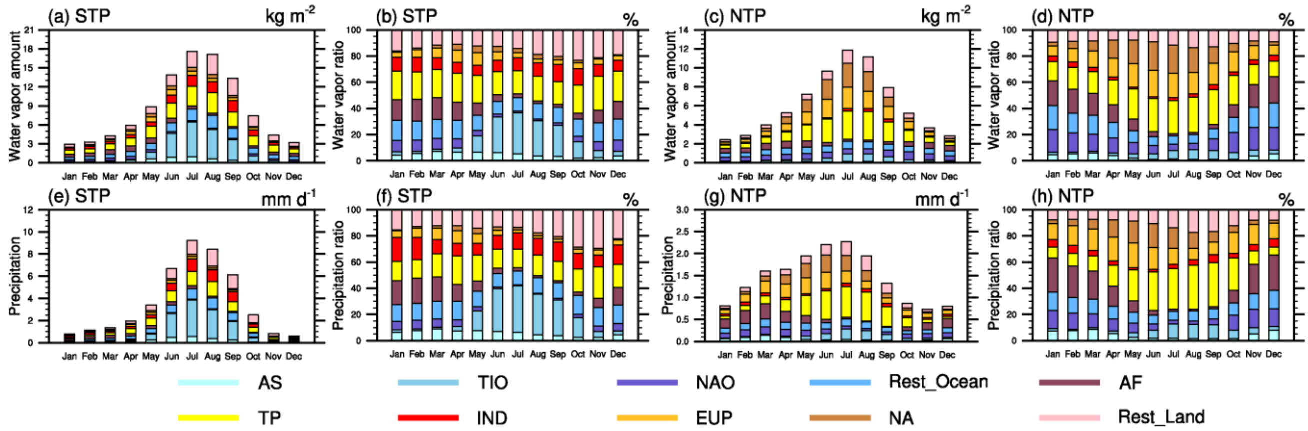

Fig. 6 (a) Monthly averaged evaporative contributions (units: kg m^{-2}) of the global source regions to the tropospheric total water vapour amount over the STP. (b) Same as (a) but for the percentage contributions (units: %) to the water vapour over the STP. (c) Monthly averaged evaporative contributions (units: kg m^{-2}) of the global source regions to the tropospheric total water vapour amount over the NTP. (d) Same as (c) but for the percentage contributions (units: %) to the water vapour over the NTP. Fig. 6e–h are same as Fig. 6a–d, respectively, but for the absolute contributions (units: mm d^{-1}) and percentage contributions (units: %) to the precipitation over the STP and NTP. Only percentage contributions of source regions to the water vapour or precipitation greater than 5 % are shown individually, with stacked column colours corresponding to the source region colours in Fig. 1. The remaining oceanic/terrestrial source regions are merged into one region, Rest_Ocean/Rest_Land

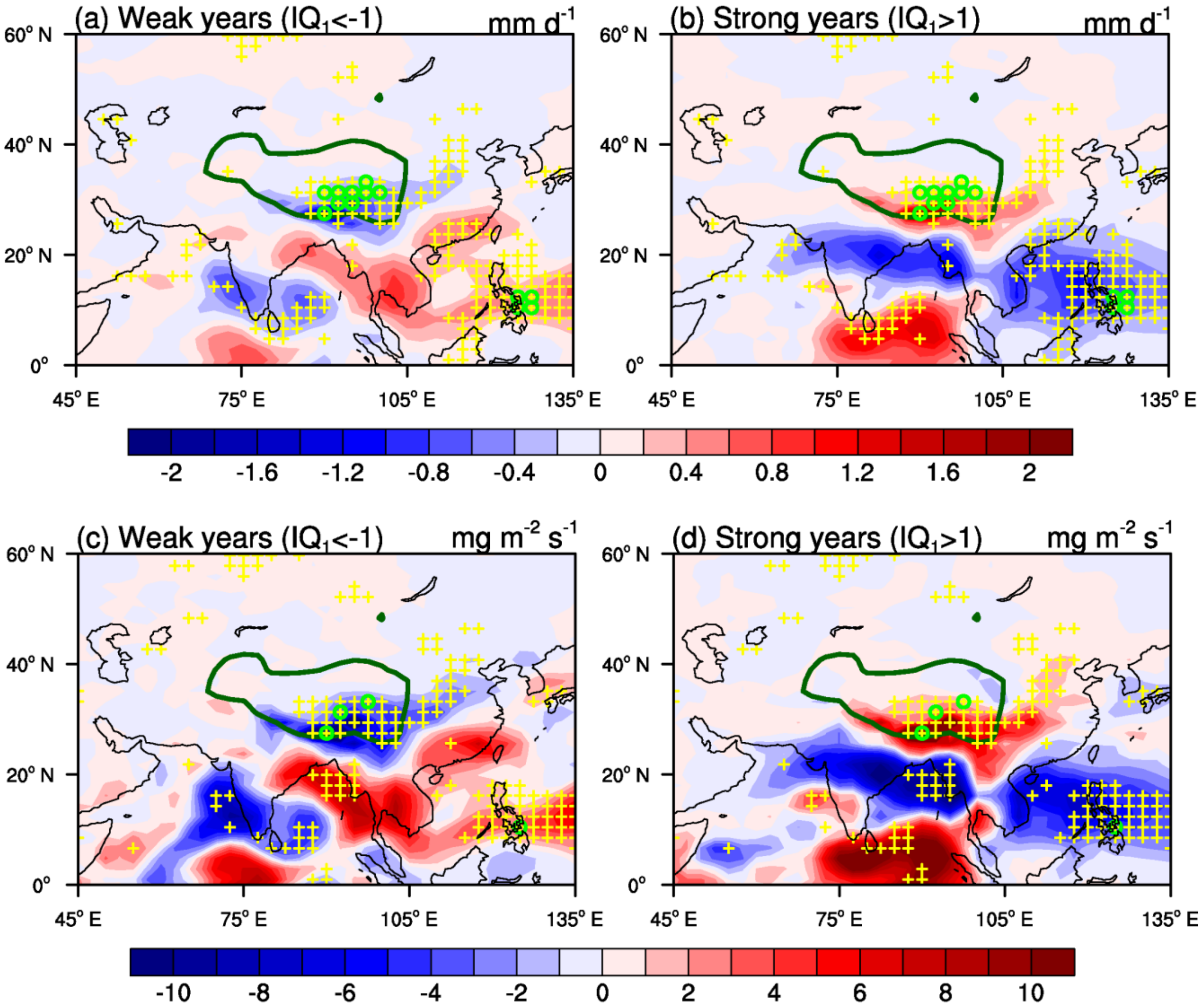

Fig. 7 (top) Composite summer mean precipitation anomalies supplied from the TIO (unit: mm d^{-1}) in the (a) five weak TP summer heating years and (b) five strong TP summer heating years. (bottom) Composite June–August mean advective tendency anomalies of water vapour that originated from the TIO (unit: mg m^{-2} s^{-1}) in the (c) five weak TP summer heating years and (d) five strong TP summer heating years. The yellow pluses indicate regions where the differences between the weak and strong composites are statistically significant at a 95 % confidence level according to a *t* test. The green circles indicate regions where the differences between the weak and strong composites satisfy the FDR criterion with α_{FDR} = 0.20. The dark-green contours indicate an orographic height of 2000 m

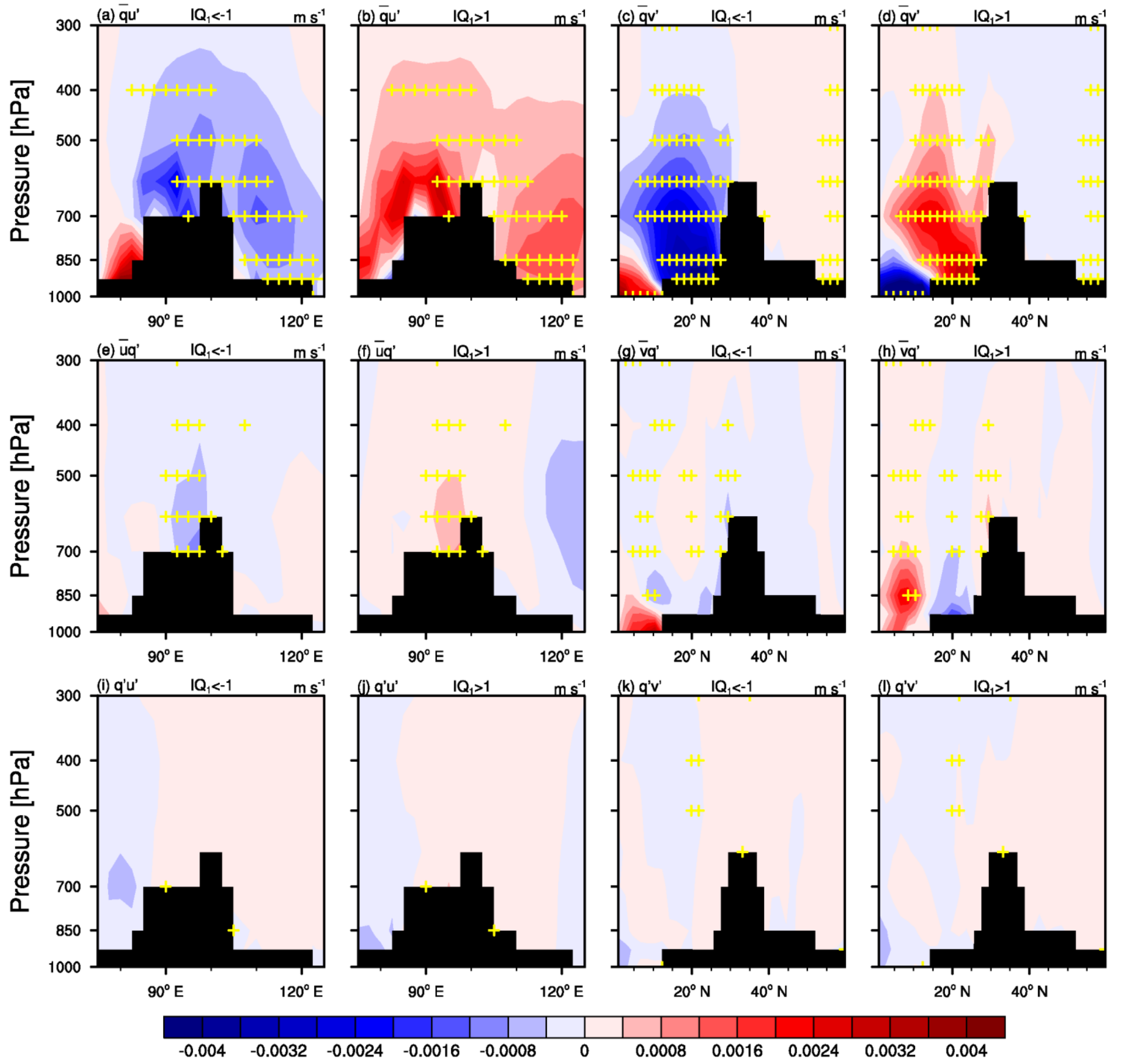

Fig. 8 (left two columns) Composite vertical profiles of the summer mean TIO-supplied zonal moisture flux components (units: m s^{-1}) in the (a, e, and i) five weak TP summer heating years and (b, f, and j) five strong TP summer heating years across a pressure-longitude cross section (27.5°–35° N average). (right two columns) Composite vertical profiles of the summer mean TIO-supplied meridional moisture flux components (units: m s^{-1}) in the (c, g, and k) five weak TP summer heating years and (d, h, and l) five strong TP summer heating years across a pressure-latitude cross section (85°–102.5° E average). The yellow pluses indicate regions where the differences between the weak and strong composites are statistically significant at a 95 % confidence level according to a *t* test. The black areas are areas with unavailable data